The Effect of ENSO on Tibetan Plateau Snow Depth: A Stationary Wave Teleconnection Mechanism and Implications for the South Asian Monsoons

JEFFREY SHAMAN

Department of Earth and Planetary Sciences, Harvard University, Cambridge, Massachusetts

ELI TZIPERMAN

Department of Earth and Planetary Sciences, and Division of Engineering and Applied Sciences, Harvard University, Cambridge, Massachusetts

(Manuscript received 30 January 2004, in final form 17 July 2004)

ABSTRACT

An atmospheric stationary wave teleconnection mechanism is proposed to explain how ENSO may affect the Tibetan Plateau snow depth and thereby the south Asian monsoons. Using statistical analysis, the short available record of satellite estimates of snow depth, and ray tracing, it is shown that wintertime ENSO conditions in the central Pacific may produce stationary barotropic Rossby waves in the troposphere with a northeastward group velocity. These waves reflect off the North American jet, turning equatorward, and enter the North African–Asian jet over the eastern Atlantic Ocean. Once there, the waves move with the jet across North Africa, South Asia, the Himalayas, and China. Anomalous increases in upper-tropospheric potential vorticity and increased wintertime snowfall over the Tibetan Plateau are speculated to be associated with these Rossby waves. The increased snowfall produces a larger Tibetan Plateau snowpack, which persists through the spring and summer, and weakens the intensity of the south Asian summer monsoons.

1. Introduction

Many facets of the global climate system have been examined for their connections with the monsoons of Asia. In particular, the effects of two large-scale phenomena, Eurasian snowpack levels and the El Niño–Southern Oscillation (ENSO), have long been explored for their interaction with Asian monsoon rainfall. The covariability of the Indian monsoons and ENSO has been examined in numerous studies (Walker 1924; Rasmusson and Carpenter 1983; Ropelewski and Halpert 1987; Webster and Yang 1992; Mehta and Lau 1997; Webster et al. 1999). During El Niño events, the Indian monsoon is generally weaker; however, recent evidence indicates this relationship may have broken down (Kumar et al. 1999).

Blanford (1884) first hypothesized that climate conditions over India could be affected by the size of the Himalayan snowpack. Changes in the size of this snowpack alter the heating of the land surface and overlying atmosphere, which in turn affects the land–sea thermal gradient and monsoon rainfall rates. Recent studies have explored the effects of both Eurasian snow cover and snow volume (depth) on the Indian monsoons. Observational investigations have demonstrated inverse relationships between Eurasian snow cover and subsequent summer rainfall over India (Hahn and Shukla 1976; Sankar-Rao et al. 1996). Kripalani et al. (1996) used satellite estimates of snow depth and found an inverse relationship between snow depth over areas of the former Soviet Union and Indian monsoon rainfall (IMR). Similarly, Bamzai and Shukla (1999) found evidence for a relationship between snow depth over central Eurasia and June–September IMR. Others have noted a dipole effect, with less western European/Russia snow depth and more central Siberia snow depth associated with greater Indian rainfall in the following season (Kripalani and Kulkarni 1999; Ye and Bao 2001). Model simulations of the global climate system have also indicated that an inverse relationship exists between snow on the Eurasian continent and Indian

Corresponding author address: Dr. Jeffrey Shaman, Department of Earth and Planetary Sciences, Harvard University, 207 Hoffman Laboratories, 20 Oxford St., Cambridge, MA 02138.
E-mail: jshaman@fas.harvard.edu

monsoon rainfall (Barnett et al. 1989; Meehl 1994; Bamzai and Marx 2000).

Snowpack levels on the Tibetan Plateau region are particularly critical to the south Asian monsoons; upper-tropospheric air temperatures above elevated land surfaces (3000–5000 m) have been demonstrated to be significantly warmer than corresponding air temperatures above surfaces at lower elevations (Molnar and Emanuel 1999). The Tibetan Plateau region (with elevations above 3000 m) supports a summertime high pressure ridge and the warmest summertime upper-tropospheric temperatures on the planet (Li and Yanai 1996). This heating of the Tibetan Plateau is integrally connected with the south Asian monsoons. Both the upper-tropospheric temperature gradient between the Himalayas and the Indian Ocean and the summertime heating of the Tibetan Plateau have been shown to be associated with the onset of the south Asian monsoons (Luo and Yanai 1984; He et al. 1987; Yanai et al. 1992; Yanai and Li 1994; Li and Yanai 1996). Furthermore, the temperature gradient between the Tibetan Plateau and equatorial Pacific has been demonstrated to be associated with Indian monsoon rainfall (Fu and Fletcher 1985), and spring snow depth on the Tibetan Plateau has been shown to be inversely associated with monsoon rainfall over Bangladesh (Shaman et al. 2005, manuscript submitted to *Int. J. Remote Sens.,* hereafter SCK).

An increased Tibetan Plateau snowpack not only increases land surface albedo, absorbed solar radiation that would otherwise have heated the land surface instead melts and sublimates the snowpack. The melting snow in turn increases land surface wetness, so that subsequent evaporation further cools the land surface. In addition, more energy is required to evaporate surface wetness; the specific heat of ice and land are about the same, but the specific heat of water is double that amount. Consequently, an increased Tibetan Plateau snowpack reduces the land–sea summer thermal gradient between the Himalayas and the Indian Ocean, consistent with the observed inverse relationship between Eurasian snowpack and the south Asian monsoons (Hahn and Shukla 1976; Dickson 1984; Ropelewski and Halpert 1989; Bamzai and Shukla 1999; SCK).

Many studies have explored the effects of snow on the monsoons, but the processes affecting Eurasian snowpack size are not fully understood. Yang (1996) found Eurasian winter snow cover to be associated with ENSO conditions such that snow cover increased during El Niño winters. Using a global atmospheric general circulation model (GCM), Meehl (1997) developed the hypothesis that the south Asian monsoons were an active component of the tropospheric biennial oscillation (TBO), and that midlatitude (Eurasian) snow cover was affected by TBO variability. This work postulated decreased Eurasian snow during an El Niño event. In another, contrasting, modeling study, Dong and Valdes (1998) found evidence that El Niño conditions lead to increased snow mass on Eurasia.

Given these conflicting findings, the processes controlling the interannual variability of the Eurasian snowpack and its relation to ENSO warrant further investigation. In this study, we focus on the relationship between Tibetan Plateau snow depth and ENSO. We examine a number of observed and reanalysis fields for connections between interannual snow depth variability over the Tibetan Plateau and ENSO. We provide evidence that spring and summer Tibetan Plateau snow depth anomalies may be the result of increased wintertime storminess over the Himalayas, and that this storminess may be modulated by ENSO. The mechanism responsible for this modulation is proposed: stationary barotropic Rossby waves with an eastward group velocity propagate from the central Pacific, over the Atlantic Ocean, and toward the Himalayas. Similar stationary barotropic Rossby waves teleconnections have been studied at length using linearized barotropic models (e.g., Sardeshmukh and Hoskins 1988), ray tracing calculations (e.g., Hoskins and Karoly 1981), and data analysis in the context of ENSO teleconnections within the Pacific (Chen 2002). We speculate here that the stationary barotropic Rossby waves excited in the atmosphere by El Niño convection reach the North African–Asian jet and cause an increase in storminess over the Himalayas, affecting snow accumulation there. The enhanced snow cover then persists to the next summer and affects the contrast in temperature between the warm air above the Tibetan Plateau and the cooler air above the Indian Ocean, which in turn affects the strength of the Indian monsoons.

Some of the logical links in the above proposed teleconnection mechanism are based on an available short (9 yr) satellite record of snow depth on the Tibetan Plateau, and are necessarily speculative for this reason. We still feel that the proposed teleconnection mechanism, supported by the other statistical analysis and ray tracing calculations in this paper, is potentially a viable explanation for some of the observed ENSO–monsoon region correlations.

In section 2 we present the data used for this study. Section 3 presents some statistical analysis of Tibetan Plateau snow depth and ENSO variability. Section 4 presents composite analyses of potential vorticity diagnostics using the National Centers for Environmental Prediction–National Center for Atmospheric Research

(NCEP–NCAR) reanalysis. Section 5 explores the proposed mechanism by which ENSO forcing may affect snowfall over the Tibetan Plateau. Section 6 provides discussion.

2. Data and methodology

a. Snow depth data

In this study we work with snow depth rather than snow cover, because both model and observational studies have shown that snow volume, or depth, is a better predictor of monsoon intensity than snow cover area (Barnett et al. 1989; Kripalani and Kulkarni 1999; Ye and Bao 2001). This finding follows from the simple thermodynamic considerations discussed in the introduction. We used the *Nimbus-7* Scanning Multichannel Microwave Radiometer (SMMR) satellite estimates of snow depth. This satellite sensor was in good operation from November 1978 to August 1987. Its passive microwave data can be used to measure snow extent and calculate snow depth on an areal basis using the difference between brightness temperatures in the 18- and 37-GHz channels (Chang et al. 1987). Monthly snow depth anomalies for the area 25°–35°N, 75°–100°E (the Himalayas and Tibetan Plateau) were determined and used.

b. ENSO and SST data

The Niño-3 region (5°N–5°S, 150°–90°W) was the index of ENSO used for this study (Kaplan et al. 1998). The global distributed SST anomaly data (5° × 5° resolution), from which the Niño-3 index is derived (Kaplan et al. 1998), were also employed.

c. NCEP–NCAR reanalysis

NCEP–NCAR reanalysis project monthly global fields for January–February–March (JFM) 1949–2002 were used in this study (Kalnay et al. 1996). Variables employed included temperature, relative vorticity, geopotential height, zonal and meridional wind speed, and streamfunction. For analysis of storm activity, daily NCEP–NCAR reanalysis project geopotential height fields for JFM 1949–2002 were high-pass filtered (<4 days) using a Butterworth filter.

d. Upper-tropospheric potential vorticity diagnosis

Maps of potential temperature at the tropopause (as identified by a surface of constant potential vorticity) are commonly used as a diagnostic of cyclogenesis in the troposphere (Hoskins et al. 1985; Davis and Emanuel 1991). The tropopause acts as an upper boundary to the troposphere; perturbations of potential temperature at the tropopause are equivalent to potential vorticity anomalies in the upper troposphere (Bretherton 1966). Thus, determination of potential temperature anomalies at the tropopause provides a powerful diagnostic tool of potential vorticity conditions within the upper troposphere.

Following the methods of Davis and Emanuel (1991), the location of the tropopause was determined using Ertel's potential vorticity (EPV):

$$q = -g(f + \zeta)\frac{d\Theta}{dp}, \tag{2.1}$$

where q is the estimate of EPV, g is the acceleration due to gravity, f is the Coriolis parameter, ζ is relative vorticity, and Θ is the potential temperature. EPV was calculated globally across all pressure levels.

Per Davis and Emanuel (1991), the tropopause was defined as the isobar of q = 1.5 PVU (1 PVU = $1e{-}6K{*}m^2\,s^{-1}\,kg^{-1}$) poleward of 10°N and 10°S. The potential temperature field was then interpolated vertically to ascertain its value at the tropopause (1.5 PVU).

TABLE 1. Seasonal lag correlations of *Nimbus-7* Tibetan Plateau snow depth within a calendar year.

	JFM	AMJ	JAS	OND
JFM	1.00	0.53	0.65	−0.47
AMJ	0.53	1.00	0.73	0.01
JAS	0.65	0.73	1.00	−0.30
OND	−0.47	0.01	−0.30	1.00

3. ENSO, snow depth accumulation, and the persistence of seasonal snow depth anomalies

In this section we use lag–lead correlations to demonstrate two main results. First, we show that winter snow depth anomalies over the Tibetan Plateau persist through the spring and summer, when snowpack size can affect the summer monsoons. Second, we provide some evidence that wintertime ENSO conditions are associated with increased snow accumulation over the Tibetan Plateau.

Table 1 presents lag autocorrelations of *Nimbus-7* Tibetan Plateau seasonal snow depth within a calendar year. These correlations indicate that snow depth anomalies indeed persist from winter to summer; Tibetan Plateau wintertime snowpack accumulation thus affects spring and summer snow depth levels. A similar tendency is found in the monthly data (data not shown). This seasonal persistence of the snow depth anomalies

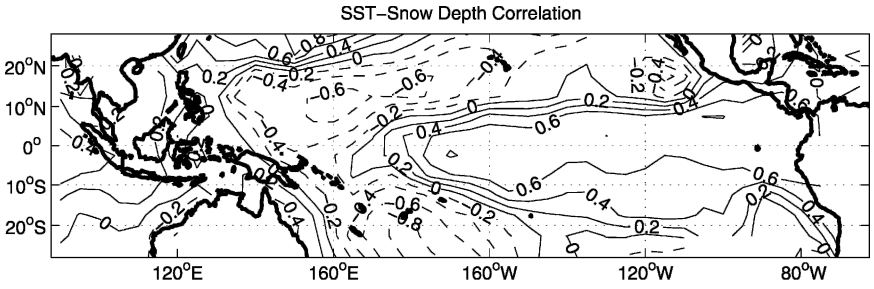

FIG. 1. Correlations of JFM SSTs with JAS Tibetan Plateau *Nimbus-7* satellite snow depth; negative correlations are dashed. The short satellite record (9 yr) most likely prevents these correlations from being statistically significant, yet the large-scale coherent structure hints at some link between Tibetan Plateau snow depth and ENSO.

is consistent with the expected thermodynamic consequences of increased snow accumulation, which further cools the land surface, as detailed in the introduction.

The *Nimbus-7* SMMR snow depth record is unfortunately very short, spanning only two complete ENSO cycles. This record length therefore does not allow rigorous statistical calculation of the linear correlation between Tibetan Plateau snow depth and the Niño-3 index. However, for qualitative purposes we have calculated the point-by-point correlation of winter (JFM) SSTs in the Pacific Ocean with summer [June–July–August (JAS)] Tibetan Plateau *Nimbus-7* snow depth. These point-by-point correlations exhibit a spatially coherent ENSO pattern (Fig. 1). That is, central and eastern tropical Pacific SSTs are positively correlated with increased Tibetan Plateau snow depth. A similar result is obtained for point-by-point correlation of winter SSTs with spring [April–May–June (AMJ)] Tibetan Plateau snow depth (not shown). This coherent spatial structure suggests a possible link between snow depth and ENSO, although the correlations presented cannot be taken as statistically significant.

While the satellite measurements suggest that Northern Hemisphere spring and summer Tibetan Plateau snow depth may be associated with Northern Hemisphere winter El Niño events, the satellite record is short and additionally provides no direct information about Northern Hemisphere winter storm activity over the Tibetan Plateau. To explore the relationship between ENSO and storm activity over the Tibetan Plateau we next correlated Northern Hemisphere winter season high-pass (<4 days) eddy variance of 200-mb geopotential height (1949–2002) with concurrent Niño-3 index values. This longer time record analysis shows that a statistically significant ($r >= 0.30$; $p < 0.05$) strong positive correlation of the Niño-3 index with high bandpass eddy geopotential variance exists over much of the Tibetan Plateau (Fig. 2). Above the Tibetan Plateau, correlations are as high as $r = 0.49$. This finding demonstrates that increased storm activity occurs over the Tibetan Plateau during Northern Hemisphere winter El Niño events. The cumulative effect of this increased JFM storm activity is apparent in the associated snow depth anomalies evident in the following seasons (Table 1; Fig. 1). In the following sections we will examine how ENSO conditions in the Pacific may affect wintertime storminess over the Tibetan Plateau and therefore the size of the spring and summer snowpacks.

4. Potential vorticity anomalies associated with snow depth and ENSO

a. Composite snow maps

We use composite maps to diagnose the wintertime atmospheric conditions associated with increased spring and summer snow depth on the Tibetan Plateau. Composite maps were constructed by plotting the averaged tropospheric winter (JFM) potential temperature during years of heavy spring or summer snow depth (based on the *Nimbus-7* data) minus that during years of light snow depth (Fig. 3). [Note that for this calculation we only represent summer by JJA rather than July–August–September (JAS) so that we can include 1987 in the composite analysis.] Heavy and light seasons were defined as +1 and −1 standard deviation, respectively. The maps show that over the Tibetan Plateau and extending eastward there is a large negative potential temperature anomaly at the tropopause during the winter season preceding both heavy spring and summer snow on the Tibetan Plateau. Shaded areas are statistically significant (see figure caption).

The region of anomalously cold potential temperature extends zonally across Asia and Africa, linking the Atlantic and Pacific Oceans (Fig. 3). These anomalies match the latitude and extent of the North African–Asian jet (Branstator 1983, 2002). This jet has been

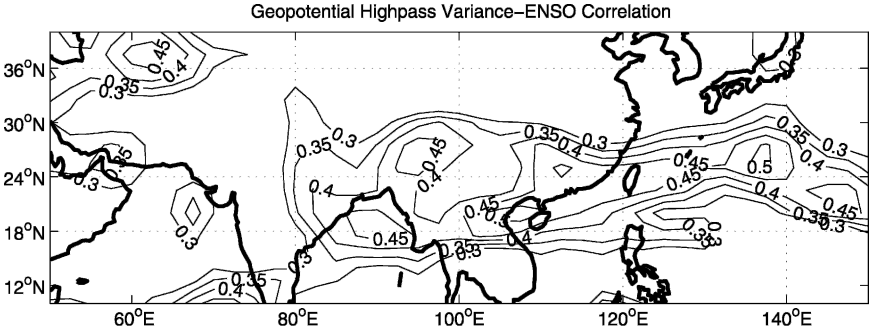

FIG. 2. Correlation of high bandpass eddy variance of JFM NCEP–NCAR reanalysis 200-mb geopotential height with concurrent Niño-3 index values (1949–2002). Only correlations of $r = 0.3$ or higher, which are significant at $p < 0.05$, are shown; the contour interval is correlation increments of 0.05.

shown to act as a waveguide, capable of connecting atmospheric activity at disparate regions of the globe; it is also associated with shifts in storm tracks and patterns of precipitation (Branstator 2002). We will now show that the cold anomaly may be due to a stationary wave pattern forced from the central and east equatorial Pacific by El Niño conditions.

b. Composite ENSO maps

In the preceding composite analyses, we observed that increased spring and summer snow depth are associated with colder winter tropopause potential temperature anomalies. We next looked to determine whether similar anomalies are associated with El Niño

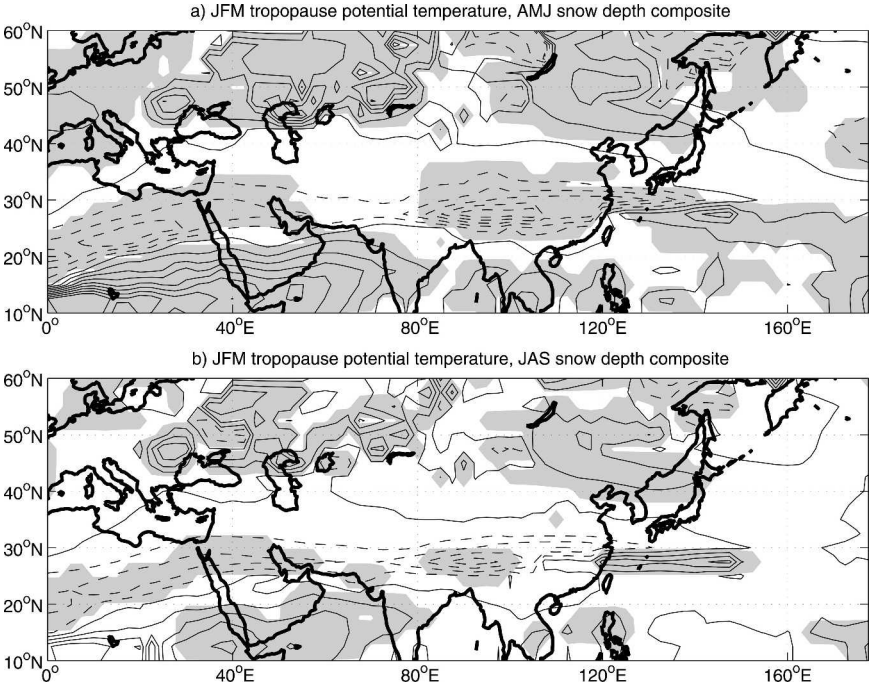

FIG. 3. Composite maps of JFM potential temperature at the tropopause (defined as 1.5 PVU) based on heavy minus light *Nimbus-7* Tibetan Plateau snow depth in the following spring and summer seasons. The height of the tropopause is determined using NCEP–NCAR reanalysis as described in the text. (a) AMJ snow depth (heavy snow: 1983; light snow: 1984, 1985); (b) JJA snow depth (heavy snow: 1982, 1983, 1987; light snow: 1984, 1985). The contour interval is 5 K. Negative contours are dashed. Shaded areas are significant ($p < 0.05$) based on bootstrap confidence intervals estimated by the generation of 5000 random composite maps from the 1979–87 JFM NCEP–NCAR reanalysis record.

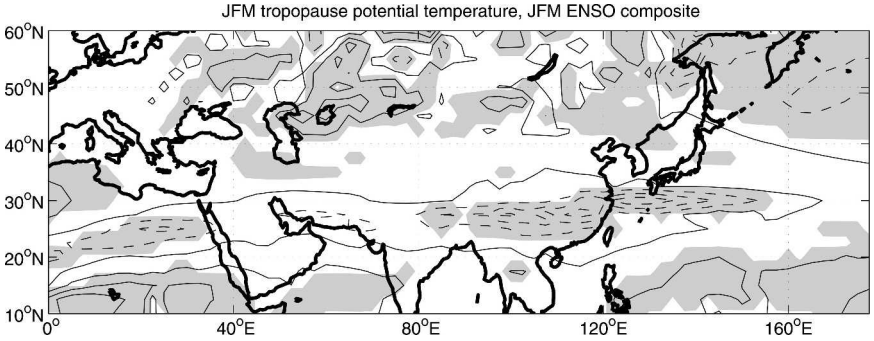

FIG. 4. Composite maps of JFM potential temperature at the tropopause (defined as 1.5 PVU) based on JFM El Niño minus La Niña event years, using the Niño-3 record (±1 standard deviation). El Niño years are 1958, 1966, 1973, 1983, 1987, 1992, and 1998; La Niña years are 1950, 1956, 1968, 1971, 1974, 1976, 1985, 1989, and 2000. The contour interval is 5 K; negative contours are dashed. Shaded areas are significant ($p < 0.05$) based on bootstrap confidence intervals estimated by generation of 5000 random composite maps from the 1949–2002 JFM NCEP–NCAR reanalysis record.

events. We examined composite maps of tropopause potential temperature during El Niño years minus La Niña years. El Niño and La Niña years were defined using the Niño-3 index (± 1 standard deviation). Figure 4 presents this composite map; once again, a cold JFM potential temperature anomaly is seen over the Tibetan Plateau and across the Asian jet, this time associated with winter El Niño conditions. The correlation of the Northern Hemisphere (0°–60°N) portion of this composite map with the heavy minus light snow year composite maps presented in Figs. 3a,b are quite high, at $r = 0.74$ and $r = 0.60$, respectively. In fashion similar to the spring and summer snow depth composite maps, the JFM tropopause potential temperature anomaly is greatest over the eastern Tibetan Plateau and extends eastward over China. The similarity between the snow composites (Fig. 3) and the ENSO composite (Fig. 4) indicates that some connection between ENSO and Tibetan Plateau snow depth may exist.

Figure 5 presents composite plots of 200-mb JFM relative vorticity for El Niño minus La Niña event years. In the central Pacific a wave train is evident emanating due north. In addition, an alternating pattern of high and low relative vorticity arcs northward and eastward from the central equatorial Pacific Ocean (a negative anomaly centered at 20°N, 145°W is followed by a positive anomaly centered over the southern United States, followed by a negative anomaly centered at 24°N, 60°W, and then a positive anomaly again centered at 15°N, 30°W); this wave train appears to turn equatorward over the United States at the latitude of the midlatitude jet stream and reaches the western coast of Africa just upstream of the North African–Asian jet. Increases in relative vorticity at 200 mb are also seen extending zonally across Africa, the Middle East, Tibet, and China. Short wave trains such as the one identified here have been analyzed previously in the context of ENSO teleconnections. Chen (2002) analyzed 3 yr of winter NCEP–NCAR reanalysis data using scale separation and identified a short wavenumber (zonal wavenumbers 4–15) wave train emanating from the subtropical West Pacific to North America, which was associated with the 1988 wintertime La Niña event.

Figure 6 shows a height–latitude cross section of the

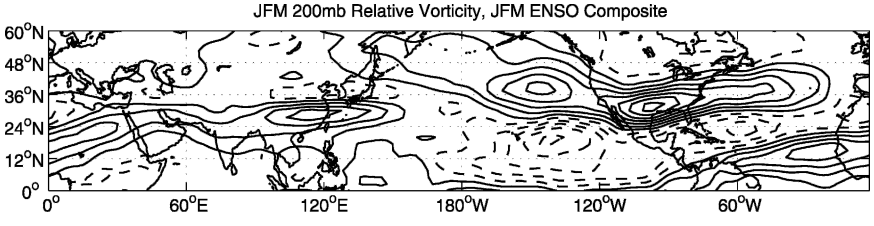

FIG. 5. The 200-mb relative vorticity composite maps based on El Niño minus La Niña event years, using the Niño-3 record (±1 standard deviation). El Niño years are 1958, 1966, 1973, 1983, 1987, 1992, and 1998; La Niña years are 1950, 1956, 1968, 1971, 1974, 1976, 1985, 1989, and 2000. Contour intervals are 5×10^{-6} s^{-1}. Negative contours are dashed.

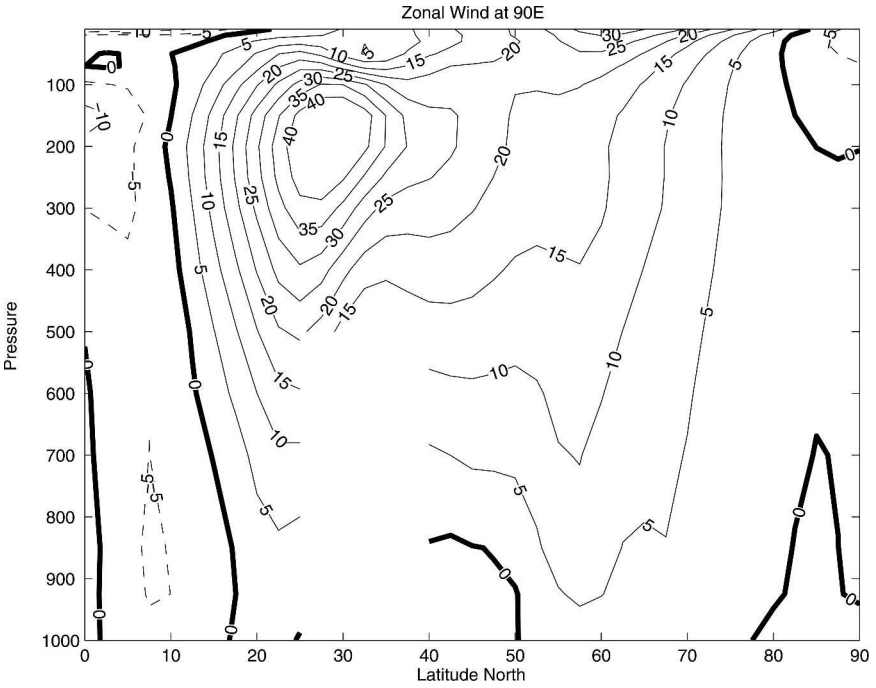

FIG. 6. Northern Hemisphere height–latitude cross section of JFM 1949–2002 zonal wind climatology for 90°E. Wind speed is given in m s^{-1}. Easterly winds are dashed.

zonal wind climatology at 90°E. The Asian jet is clearly revealed as the zone of strong westerly winds centered at 30°N and 200 mb. Prevailing westerly winds occur down to 500 mb (surface level on the Tibetan Plateau). Air masses advected from the west at higher pressure levels (nearer the surface) upon approaching the Tibetan Plateau area, will encounter the above colder tropopause potential temperature anomalies such as seen in Fig. 4. A cold anomaly at the tropopause is equivalent to an increased upper-tropospheric potential vorticity anomaly (Bretherton 1966). Hoskins et al. (1985) have suggested that air advected from the west toward such an anomaly would be subject to vertical motions that would lead to increased cloudiness and precipitation on the western edge of the anomaly. This sequence of events is one possible explanation for the observed increased storm activity seen in Fig. 2.

5. A stationary wave mechanism linking ENSO and Tibetan Plateau snow

a. Extratropical response

The above composite analyses based on winter ENSO conditions highlight the response of the atmosphere to anomalous thermal forcing in the central and eastern Pacific due to El Niño conditions. Atmospheric responses to thermal forcing have been examined in great detail (Hoskins and Karoly 1981; Branstator 1983; Simmons et al. 1983; Sardeshmukh and Hoskins 1988; Lau and Peng 1992; Hoskins and Ambrizzi 1993; Ambrizzi et al. 1995). Hoskins and Karoly (1981), Branstator (1983), and Hoskins and Ambrizzi (1993) have explored the atmospheric response to subtropical and equatorial thermal forcing using ray tracing and linearized barotropic and baroclinic models of Northern Hemisphere wintertime conditions. These studies found that low-latitude thermal forcing excites barotropic Rossby waves in the midlatitude troposphere; these barotropic stationary waves are characterized by poleward and eastward group velocities with longer wavenumbers traveling more poleward. Shorter wavenumbers ($k > 3$) are refracted by the jet stream and turn back toward the equator. Hoskins and Karoly (1981) showed that for a forcing at 15°N, stationary wavenumbers 4–6 traveled poleward and eastward to 30°–40°N, then turned equatorward and eastward, returning to 15°N about 90°E of the forcing. Hoskins and Ambrizzi (1993) showed that an equatorial forcing in the eastern Pacific, excited Rossby waves of wavenumber 4–6 that followed a similar arcing pattern. As noted before, a similar response is seen in the ENSO composite analysis shown in Fig. 5.

Once off the west coast of North Africa, eastward-propagating waves can enter the North African–Asian jet. Figure 7 presents JFM climatology (1949–2002) of the meridional gradient of potential vorticity, as well as

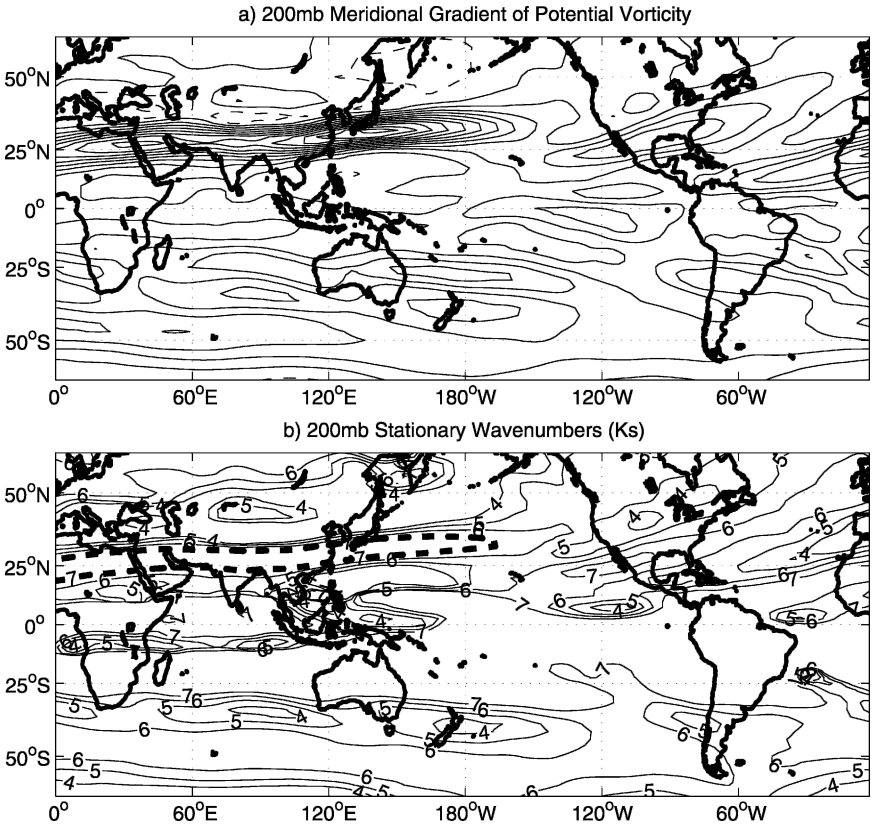

FIG. 7. (a) JFM 200-mb meridional gradient of potential vorticity; the contour interval is 1×10^{-11} m^{-1} s^{-1}; zero and negative contours are dashed. (b) Stationary wavenumbers [Eq. (5.1)]. Wavenumbers 4, 5, 6, and 7 are plotted. Wavenumber 7 is drawn thickened and dashed to highlight the North African–Asian jet. This contour is flanked closely by lower wavenumber contours and thus illustrates how higher wavenumber Rossby waves refract toward the jet center. Both plots are derived from the 1949–2002 NCEP–NCAR reanalysis climatology.

the stationary wavenumbers as a function of location, calculated as (Hoskins and Ambrizzi 1993)

$$K_s = \left(\frac{\beta - \partial^2 \overline{u}/\partial y^2}{\overline{u}} \right)^{1/2}, \qquad (5.1)$$

where K_s is the local stationary wavenumber, $\overline{u}(y)$ is the time mean zonal wind, β is the change in the Coriolis parameter with latitude, and y is latitude. There is a large maximum in the meridional gradient of potential vorticity that demarcates the North African–Asian jet. This jet is also apparent as a zonal band of maximum stationary wavenumbers flanked by lower stationary wavenumbers to the north and south (Fig. 7b). As shown by Hoskins and Ambrizzi (1993), Rossby rays refract toward latitudes with larger K_s. Thus, stationary Rossby waves within the jet will remain trapped and propagate zonally across North Africa, the Middle East, the Tibetan Plateau and China, that is, the entire length of the jet.

Conversely, stationary Rossby waves outside the North African–Asian jet cannot enter midway from the north or south, but must instead enter the jet at its inception west of Africa. Thus, waves excited by convection in the central and eastern Pacific may propagate eastward into the entrance of the North African–Asian jet and alter wintertime snowpack accumulation on the Tibetan Plateau. We next show that this speculated wave propagation from the ENSO region to the monsoons region is supported by ray tracing calculations.

b. *Two-dimensional ray tracing*

The preceding analysis of stationary wavenumbers (Fig. 7) provides a conceptual basis for understanding barotropic Rossby wave propagation behavior in the real atmosphere. Furthermore, it suggests that the ENSO composite relative vorticity anomalies seen in Fig. 5 may be the result of stationary barotropic Rossby

wave propagation. From 180° to 0° the relative vorticity anomalies evident in Fig. 5 are remarkably similar to the forced solution of a linear vorticity equation model employed by Sardeshmukh and Hoskins (1988, hereafter SH88). The forcing in the SH88 model was centered at 5°S, 235°E, using a 150-mb wintertime (December 1985–February 1986) mean flow as the basic state. The streamfunction response found in these forced linear simulations (Fig. 7e of SH88) is quite similar to that seen for the ENSO composite relative vorticity anomaly pattern presented here (Fig. 5). Both patterns resemble a wave train of zonal wavenumber 4 moving northeastward from the forcing, reflecting off the North American jet, and moving southeastward over the Atlantic to the entrance of the North African–Asian jet.

To further explore this possible wave train, we next performed Rossby wave ray tracing in the JFM 200-mb time-mean atmosphere, accounting for both zonal and meridional variations of flow. For this exercise, we follow the general theory of ray tracing in an anisotropic system (Whitham 1974; Lighthill 1978). Following Karoly (1983), we consider solutions to the nondivergent barotropic, quasigeostrophic vorticity equation linearized about a time-mean basic state with streamfunction $\overline{\psi}(x, y)$. Within this framework the equation for the perturbation streamfunction on a Mercator projection of a sphere yields the following dispersion relation:

$$\omega = \overline{u}_M k + \overline{v}_M l + \frac{(l\partial\overline{q}/\partial x - k\partial\overline{q}/\partial y)}{k^2 + l^2}, \qquad (5.2)$$

where $(\overline{u}_M, \overline{v}_M) = ((\overline{u}, \overline{v})/\cos\theta)$ is the Mercator projection of the time-mean zonal and meridional winds; θ is latitude; k and l are wavenumbers in the zonal and meridional directions, respectively; and $\overline{q} = f_0 + \beta y + \nabla^2\overline{\psi}$ is the time-mean absolute vorticity. Using (5.2), the path of a wave ray is found by integrating the four equations for the path (x, y) and for the changing wavenumbers (k, l) (Karoly 1983). For time-mean fields, we used the 1949–2002 climatological NCEP–NCAR reanalysis JFM winds. This field was smoothed using a low-pass Butterworth filter.

The ray tracings were initiated with integer zonal wavenumbers $k = 1$–7 at forcing sites in the central and eastern equatorial Pacific. Initial meridional wavenumbers, l, were determined using the dispersion relation (5.2) and values of $\overline{u}_M$, $\overline{v}_M$, $\partial\overline{q}/\partial x$, and $\partial\overline{q}/\partial y$ at the initial point of the ray path (i.e., the forcing location for the waves), assuming a zero frequency (stationary waves). The integrations for the ray paths were terminated after 15 days. Figure 8 presents representative rays for several forcing sites and wavenumbers. Rossby wave rays moving initially northward and eastward are reflected off the jet over North America and enter the North African–Asian jet west of Africa. The ray path matches the arching pattern of anomalies in the 200-mb relative vorticity composite anomalies for El Niño minus La Niña event years. Once in the North African–Asian jet, the rays remain confined and propagate eastward over South Asia and the Himalayas. The majority of forcing locations between 0°–10°N and 150°–120°W with initial zonal wavenumbers 4 and 5 produced similar responses. Many forcings with initial zonal wavenumbers 1, 2, 3, and 6 also produced stationary Rossby waves that entered the North African–Asian jet.

While there is no clear stationary wave pattern of positive and negative vorticity anomalies within the North African–Asian jet (see Figs. 4 and 5) there does appear a single-signed increase of relative vorticity superimposed on a wave pattern of wavenumber 4. A number of effects within the jet could be obscuring the development of a clearer stationary wave pattern and leading to this single-signed structure within the jet. These effects include wave–mean flow interaction and energy conversion (Li and Nathan 1997) and the fact that different initial zonal wavenumber Rossby rays (1–6) enter the jet and become superpositioned.

The forced linear solution of SH88 (forcing centered at 5°S, 235°E, using a 150-mb wintertime mean flow as the basic state; Fig. 7e in SH88) provides evidence of similar stationary Rossby wave propagation from the central and eastern Pacific to the entrance of the North African–Asian jet. However, the SH88-forced solution gives no clear delineation of a wave train in the North African–Asian jet; rather, there are negative streamfunction anomalies over Arabia and southeast China (analogous to the positive relative vorticity anomalies we present in Figs. 5 and 8 here), while in between these anomalies where the jet flows there is effectively zero streamfunction anomaly. This discrepancy in the North African–Asian jet region between the SH88-forced solution streamfunction anomalies and the ENSO composite relative vorticity anomalies shown here in Fig. 5 may be explained by the SH88 vorticity model formulations, which ignore vertical advection and twisting terms in the vorticity balance. As SH88 point out, these terms are "not insignificant in the jet stream regions." The forced solution of the SH88 linear model therefore likely inadequately describes the response in the North African–Asian jet while better capturing the atmospheric response upstream of the jet. Thus, the SH88-forced solution appears to corroborate the results and teleconnection we present here.

The ray tracing calculations hint at the possible

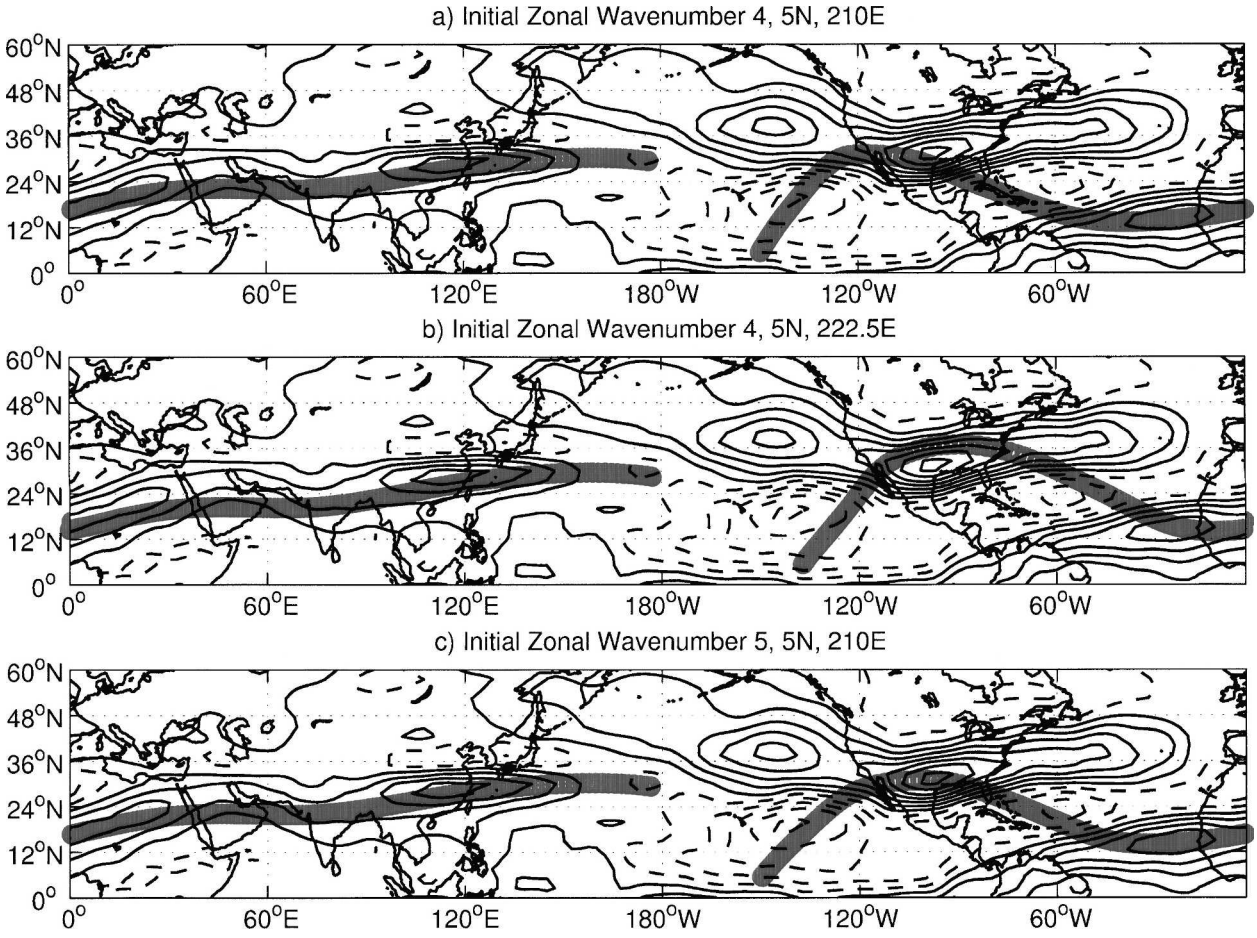

FIG. 8. Ray tracings of barotropic Rossby waves propagating eastward from the central Pacific to the Indian monsoon area. The 1949–2002 NCEP–NCAR reanalysis JFM climatology is used as the basic state. Plots of the ray paths are superimposed on the 200-mb relative vorticity composite maps based on El Niño minus La Niña event years also shown in Fig. 5. (a) The path of a Rossby ray, starting with an initial zonal wavenumber 4 at 5°N, 210°E, and following the wave for 15 days; (b) same as (a), starting with an initial zonal wavenumber 4 at 5°N, 222.5°E; (c) same as (a), starting with an initial zonal wavenumber 5 at 5°N, 210°E.

means of signal propagation from the equatorial Pacific to the Tibetan Plateau, and a teleconnection mechanism from ENSO to the monsoons. Convection in the central and eastern equatorial Pacific, associated with El Niño conditions, produces northward- and eastward-propagating stationary barotropic Rossby waves. These waves reflect off the midlatitude jet over North America, head equatorward over the Atlantic Ocean, and then enter the North African–Asian jet. Within this jet, the wave energy moves across North Africa, south Asia, the Himalayas, and China, all the way to the Tibetan Plateau.

We can now further speculate that anomalous upper-tropospheric conditions induced by these Rossby waves over the Tibetan Plateau favor convection and wintertime snowfall, as hinted by the similarity of the composite maps for ENSO and snow depth (Figs. 3 and 4). This increased snowfall over the Tibetan Plateau produces a larger snowpack, which persists through the spring and summer and affects the south Asian monsoons.

6. Discussion

We examined the effects of Northern Hemisphere wintertime ENSO conditions on snow depth over the Tibetan Plateau. Using the available short record of *Nimbus-7* satellite seasonal snow depth estimates, high-pass eddy 200-mb geopotential variance, and the Niño-3 index we have shown that Northern Hemisphere winter storm activity and consequent spring and summer snow depth on the Tibetan Plateau appear correlated with JFM Pacific Ocean SSTs in that same year.

A mechanism explaining this connection has been proposed. During an El Niño event, stationary barotropic Rossby waves with an eastward group velocity escape northward and eastward from the central equatorial Pacific, but are then reflected equatorward from the midlatitude jet and enter the North African–Asian jet, where they remain trapped in a narrow meridional band. The anomalous stationary barotropic Rossby waves entering the North African–Asian jet during El Niño events seem to affect conditions within the jet, and may be associated with increased storminess over the Tibetan Plateau. This wintertime storminess leads to increased snow accumulation through the winter and increased snow depth in the following spring and summer seasons.

An increased spring and summer snowpack on the Tibetan Plateau diminishes the meridional land–sea thermal gradient that drives the south Asian monsoons. Thus, a strong wintertime El Niño would be associated with a weak south Asian monsoon during the following summer, which is generally the case for India (Walker 1924; Rasmusson and Carpenter 1983; Ropelewski and Halpert 1987; Webster and Yang 1992; Mehta and Lau 1997; Webster et al. 1999).

The vorticity anomalies observed within the North African–Asian jet during El Niño events may increase Tibetan Plateau storminess and rates of wintertime snow accumulation in a number of ways. The interaction of the westerly winds and the vorticity anomalies in the upper troposphere above the Tibetan Plateau (Fig. 5) is one possible explanation for the increased storm activity (Hoskins et al. 1985). Alternatively, it has been demonstrated that low-frequency barotropic alterations of the atmosphere, such as shown here in the North African–Asian jet during El Niño events, can create an altered steering effect sufficient to explain storm activity anomalies (Branstator 1995). Local changes in baroclinicity may also occur and affect storm frequency, and shifts in the jet, such as the southward shift of the North African–Asian jet associated with El Niño events (data not shown), could result in more disturbances reaching the Tibetan Plateau. These effects may act individually or in consort, and no doubt are influenced by Himalayan orography.

The present work was limited to the telecommunication between ENSO and the Himalayas during the Northern Hemisphere winter. We may further speculate, however, that during the Northern Hemisphere summer, telecommunication between ENSO and the monsoons also occurs (Shaman and Tziperman 2005, manuscript submitted to *J. Climate*). Thus, the effect of ENSO on the monsoons may be twofold. Wintertime conditions in the Pacific affect snowpack accumulation on the Tibetan Plateau via eastward-propagating Rossby waves. In addition, during the Northern Hemisphere summer monsoons, the state of ENSO may influence monsoon rainfall more directly via alteration of circulation, temperature, and subsidence patterns within the Tropics. From this perspective both the time of year and the strength of the ENSO event are important for determining the monsoon response.

The monsoons are the result of interactions among large, persistent, regional components of the global climate system (Tibetan Plateau snow, ENSO, Indian Ocean SSTs) at different times of the year. The mechanism identified here shows how conditions in one season (Northern Hemisphere wintertime ENSO) may affect those in another (spring and summer Tibetan Plateau snow depth and, by extension, south Asian monsoon intensity). At present, GCM representation of the Asian monsoons is generally poor (Sperber et al. 2001). Mean seasonal rainfall levels are not well represented, nor are interannual and intraseasonal variability. Furthermore, the relationship between Indian rainfall and ENSO in GCM simulations is often of the wrong sign. However, using mechanisms such as the one identified here, simpler dynamic predictive models might be constructed. To build such models, and better understand the monsoons, further research is needed to elucidate the interactions of regional components of the monsoon system.

Acknowledgments. This research was supported by the NOAA Postdoctoral Program in Climate and Global Change, administered by the University Corporation for Atmospheric Research (for JS), by the McDonnell Foundation and by the NSF Climate Dynamics program Grant ATM 0351123. We thank M. Cane, K. Emanuel, L. Illari, and Y. Kushnir for helpful discussions.

REFERENCES

Ambrizzi, T., B. J. Hoskins, and H.-H. Hsu, 1995: Rossby wave propagation and teleconnection patterns in the austral winter. *J. Atmos. Sci.,* **52,** 3661–3672.

Bamzai, A. S., and J. Shukla, 1999: Relation between Eurasian snow cover, snow depth, and the Indian summer monsoon: An observational study. *J. Climate,* **12,** 3117–3132.

——, and L. Marx, 2000: COLA AGCM simulation of the effect of anomalous spring snow over Eurasia on the Indian summer monsoon. *Quart. J. Roy. Meteor. Soc.,* **126,** 2575–2584.

Barnett, T. P., L. Dumenil, U. Schlese, E. Roeckner, and M. Latif, 1989: The effect of Eurasian snow cover on regional and global climate variations. *J. Atmos. Sci.,* **46,** 661–685.

Blanford, H. F., 1884: On the connexion of Himalayan snowfall

and seasons of drought in India. *Proc. Roy. Soc. London,* **37,** 3–22.

Branstator, G., 1983: Horizontal energy propagation in a barotropic atmosphere with meridional and zonal structure. *J. Atmos. Sci.,* **40,** 1689–1708.

——, 1995: Organization of storm track anomalies by recurring low-frequency circulation anomalies. *J. Atmos. Sci.,* **52,** 207–226.

——, 2002: Circumglobal teleconnections, the jet stream waveguide, and the North Atlantic Oscillation. *J. Climate,* **15,** 1893–1910.

Bretherton, F. P., 1966: Critical layer instability in baroclinic flows. *Quart. J. Roy. Meteor. Soc.,* **92,** 325–334.

Chang, A., J. L. Foster, and D. K. Hall, 1987: *Nimbus-7* derived global snow cover parameters. *Ann. Glaciol.,* **9,** 39–45.

Chen, T.-C., 2002: A North Pacific short-wave train during the extreme phases of ENSO. *J. Climate,* **15,** 2359–2376.

Davis, C. A., and K. A. Emanuel, 1991: Potential vorticity diagnostics of cyclogensis. *Mon. Wea. Rev.,* **119,** 1929–1953.

Dickson, R. R., 1984: Eurasian snow cover versus Indian monsoon rainfall—An extension of the Hahn–Shukla results. *J. Climate Appl. Meteor.,* **23,** 171–173.

Dong, B. W., and P. J. Valdes, 1998: Modelling the Asian summer monsoon rainfall and Eurasian winter/spring snow mass. *Quart. J. Roy. Meteor. Soc.,* **124B,** 2567–2596.

Fu, C., and J. O. Fletcher, 1985: The relationship between Tibet-tropical ocean thermal contrast and the interannual variability of Indian monsoon rainfall. *J. Climate Appl. Meteor.,* **24,** 841–847.

Hahn, D. G., and J. Shukla, 1976: Apparent relationship between Eurasian snow cover and Indian monsoon rainfall. *J. Atmos. Sci.,* **33,** 2461–2462.

He, H., J. W. McGinnis, Z. Song, and M. Yanai, 1987: Onset of the Asian summer monsoon in 1979 and the effect of the Tibetan Plateau. *Mon. Wea. Rev.,* **115,** 1966–1995.

Hoskins, B. J., and D. J. Karoly, 1981: The steady linear response of a spherical atmosphere to thermal and orographic forcing. *J. Atmos. Sci.,* **38,** 1179–1196.

——, and T. Ambrizzi, 1993: Rossby wave propagation on a realistic longitudinally varying flow. *J. Atmos. Sci.,* **50,** 1661–1671.

——, M. E. McIntyre, and A. W. Robertson, 1985: On the use and significance of isentropic potential vorticity maps. *Quart. J. Roy. Meteor. Soc.,* **111,** 877–947.

Kalnay, E., and Coauthors, 1996: The NCEP/NCAR 40-Year Reanalysis Project. *Bull. Amer. Meteor. Soc.,* **77,** 437–471.

Kaplan, A., M. Cane, Y. Kushnir, A. Clement, B. Blumenthal, and B. Rajagopolan, 1998: Analyses of global sea surface temperature 1856–1991. *J. Geophys. Res.,* **103C,** 18 567–18 589.

Karoly, D. J., 1983: Rossby-wave propagation in a barotropic atmosphere. *Dyn. Atmos. Oceans,* **7,** 111–125.

Kripalani, R. H., and A. Kulkarni, 1999: Climatology and variability of historical Soviet snow depth data: Some new perspectives in snow–Indian monsoon teleconnections. *Climate Dyn.,* **15,** 475–489.

——, S. V. Singh, A. D. Vernekar, and V. Thapliyal, 1996: Empirical study on *Nimbus-7* snow mass and Indian summer monsoon rainfall. *Int. J. Climatol.,* **16,** 23–34.

Kumar, K., R. Kleeman, M. A. Cane, and B. Rajagopalan, 1999: Epochal changes in Indian monsoon–ENSO precursors. *Geophys. Res. Lett.,* **26,** 75–78.

Lau, K.-M., and L. Peng, 1992: Dynamics of atmospheric teleconnections during the northern summer. *J. Climate,* **5,** 140–158.

Li, C., and M. Yanai, 1996: The onset and interannual variability of the Asian summer monsoon in relation to land–sea thermal contrast. *J. Climate,* **9,** 358–375.

Li, L., and T. R. Nathan, 1997: Effects of low-frequency tropical forcing on intraseasonal tropical–extratropical interactions. *J. Atmos. Sci.,* **54,** 332–346.

Lighthill, J., 1978: *Waves in Fluids.* Cambridge University Press, 504 pp.

Luo, H., and M. Yanai, 1984: The large-scale circulation and heat sources over the Tibetan Plateau and surrounding areas during the early summer of 1979. Part II: Heat and moisture budgets. *Mon. Wea. Rev.,* **112,** 966–989.

Meehl, G. A., 1994: Coupled land–ocean–atmosphere processes and South Asian monsoon variability. *Science,* **266,** 263–267.

——, 1997: The south Asian monsoon and the tropospheric biennial oscillation. *J. Climate,* **10,** 1921–1943.

Mehta, V. M., and K.-M. Lau, 1997: Influence of solar irradiance on the Indian monsoon–ENSO relationship at decadal–multidecadal time scales. *Geophys. Res. Lett.,* **24,** 159–162.

Molnar, P., and K. A. Emanuel, 1999: Temperature profiles in radiative–convective equilibrium above surfaces at different heights. *J. Geophys. Res.,* **104,** 24 265–24 271.

Rasmusson, E. M., and T. H. Carpenter, 1983: The relationship between eastern equatorial Pacific sea surface temperatures and rainfall over India and Sri Lanka. *Mon. Wea. Rev.,* **111,** 517–528.

Ropelewski, C. F., and M. S. Halpert, 1987: Global and regional scale precipitation patterns associated with the El Niño/Southern Oscillation. *Mon. Wea. Rev.,* **115,** 1606–1626.

——, and ——, 1989: Precipitation patterns associated with the high index phase of the Southern Oscillation. *J. Climate,* **2,** 268–284.

SankarRao, M., K. M. Lau, and S. Yang, 1996: On the relationship between Eurasian snow cover and the Asian summer monsoon. *Int. J. Climatol.,* **16,** 605–616.

Sardeshmukh, P. D., and B. J. Hoskins, 1988: The generation of global rotational flow by steady idealized tropical divergence. *J. Atmos. Sci.,* **45,** 1228–1251.

Simmons, A. J., J. M. Wallace, and G. W. Branstator, 1983: Barotropic wave propagation and instability, and atmospheric teleconnection patterns. *J. Atmos. Sci.,* **40,** 1363–1392.

Sperber, K. R., and Coauthors, 2001: Dynamical seasonal predictability of the Asian summer monsoon. *Mon. Wea. Rev.,* **129,** 2226–2248.

Walker, G. T., 1924: Correlation in seasonal variations of weather. IV: A further study of world weather. *Mem. Indian Meteor. Dept.,* **24,** 275–332.

Webster, P. J., and S. Yang, 1992: Monsoon and ENSO—Selectively interactive systems. *Quart. J. Roy. Meteor. Soc.,* **118,** 877–926.

——, A. M. Moore, J. P. Loschnigg, and R. R. Leben, 1999: Coupled ocean–atmosphere dynamics in the Indian Ocean during 1997–98. *Nature,* **401,** 356–360.

Whitham, G. B., 1974: *Linear and Nonlinear Waves.* John Wiley and Sons, 636 pp.

Yanai, M., and C. Li, 1994: Mechanism of heating and the boundary layer over the Tibetan Plateau. *Mon. Wea. Rev.,* **122,** 305–323.

——, ——, and Z. Song, 1992: Seasonal heating of the Tibetan Plateau and its effects on the evolution of the Asian summer monsoon. *J. Meteor. Soc. Japan,* **70,** 319–351.

Yang, S., 1996: ENSO–snow–monsoon associations and seasonal–interannual predictions. *Int. J. Climatol.,* **16,** 125–134.

Ye, H. C., and Z. H. Bao, 2001: Lagged teleconnections between snow depth in northern Eurasia, rainfall in Southeast Asia and sea-surface temperatures over the tropical Pacific Ocean. *Int. J. Climatol.,* **21,** 1607–1621.